Direct synthesis of sodium doped Cu_2O/GO nanocomposites for catalytic hydrogen production from $NaBH_4$

Khulaif Alshammari[1*], Sultan Alhassan[1], Alhulw H. Alshammari[1], Turki Alotaibi[1], Majed Alshammari[1], T. A. Taha[1] , Satam Alotibi[2] and Mohamed Henini[3]

[1]Physics department, College of Science, Jouf University, P.O. Box:2014, Sakaka, Saudi Arabia
[2]Department of Physics, College of Science and Humanities in Al-Kharj, Prince Sattam bin Abdulaziz University, Al-Kharj 11942, Saudi Arabia
[3]School of Physics and Astronomy, University of Nottingham, Nottingham NG7 2RD, UK

[*]**Correspondence: Email address; knnalshammari@ju.edu.sa**

Abstract

In this work, Cu_2O/GO doped Na nanocomposites were prepared via sol-gel auto-combustion procedure. The material structure was analysed using X-ray diffraction (XRD), Fourier transform infrared spectroscopy (FTIR) and environmental scanning electron microscopy (ESEM). The crystal structure of the Cu_2O/GO, $Cu_{1.7}Na_{0.3}O$/GO and $Cu_{1.4}Na_{0.6}O$/GO nanocomposites was found to be cubic as evidenced by XRD patterns. The complexing of copper oxide and GO was confirmed by FTIR and Raman spectroscopy. ESEM micrographs showed that Cu_2O nanoparticles are integrated into GO nanosheets. The surface area of these nanocomposites decreased from 122 to 59 m^2/g. The optical energy gap was found to decrease from 2.14 to 1.72 eV with increasing sodium content. The addition of sodium to Cu_2O/GO nanocomposites accelerated the hydrogen evolution from $NaBH_4$. The maximum rate of hydrogen (10981 mL/g.min) was achieved for the $Cu_{1.4}Na_{0.6}O$/GO nanocomposite sample. These findings confirm that the prepared nanocomposites could be used as efficient hydrogen catalysts.

Keywords: Cu_2O/GO nanocomposites; Energy gap; Hydrogen gas; $NaBH_4$

1. Introduction

The accumulated global warming problem has stimulated the provision of alternative energy sources. Renewable energy sources, which are abundant all around us, are replenished by the sun, wind, water, waste, and Earth's heat. However, hydrogen energy has recently attracted attention as a good alternative. Hydrogen is the most abundant chemical element in the universe. The combustion of hydrogen will not cause harmful emissions to the environment [1]. Many industrial bodies are seeking to produce large quantities of hydrogen. Catalysts are used to increase the production of hydrogen from water as well as from metal hydrides. There have been many attempts to produce cheap and high-efficiency catalysts. Metal oxides represent a good alternative because of their low cost, ease of preparation, and wide range of applications [2-5]. In addition, metal oxides combined with carbon nanomaterials possess high electrical conductivity and improved optical properties [5]. One of the most important forms of carbon is graphene, which forms a two-dimensional carbon sheet with strong covalent bonds between each carbon atom [6-8]. Graphene has a large surface area with promising optical and mechanical properties suitable for a wide range of applications [9]. However, it has been shown that graphene suffers from thermodynamic limitations. For this reason, great efforts have been made to oxidize graphene to eliminate these defects. Graphene oxide (GO) contains oxygen functional groups, such as hydroxyl, carboxyl, and carbonyl [10]. The presence of these functional groups contributes to the binding of graphene to the nano-metal oxides [11]. Previous studies demonstrated that metal oxide/GO composites can achieve high performance in catalyst and energy storage applications [12,13].

Copper oxide (Cu_2O) has a cubic crystal structure and shows improved optical and electrical properties when the dimensions are reduced to nano sizes [14]. Furthermore, Cu_2O has an energy gap of 2.17 eV which qualifies it for many applications such as photovoltaics, optoelectronics, and photocatalysis [15-16]. Moreover, Cu_2O shows high corrosion resistance and high thermal and mechanical stability in various media [17].

The use of catalysts for hydrogen production has attracted great interest, especially sodium borohydride ($NaBH_4$) catalysis reactions. The importance of $NaBH_4$ is due to its high stability in fuel cells. Interestingly, sodium represents a safe material for hydrogen storage. The

decomposition of $NaBH_4$ in methanol is a recyclable method unlike hydrolysis in water. These reactions produce hydrogen gas and a byproduct of sodium metaborate ($NaBO_2$). If methanol is used, it can be recycled, and the byproduct compounds can be easily removed. Further, methanol provides spontaneous hydrogen production at a low reaction temperature. Methanol, among the various alcohols, allows the generation of high density H_2 gas [18].

Previous work showed variations in the performance of metal oxide catalysts for hydrogen production. Ni/TiO_2 catalyst material, which was prepared by sol-gel method, achieved a H_2 generation rate of 110.87 mL/g.min [19]. Co_3O_4 microcubes catalysts, Co_3O_4 nanorods, Co_3O_4 nanofoams and FeCuCo matrials produced a production rate of 1497 mL/g.min [20], 1776 mL/g.min [21], 1930 mL/g.min [22], and 1380 mL/g.min [23], respectively. Fe_2O_3/MWCNT (multi-walled carbon nanotubes) composite was employed as a catalyst for $NaBH_4$ hydrogenation and showed a production rate of 1368 mL in 140 min [24].

The current work has two objectives, namely, to prepare $Cu_{2-x}Na_xO$/GO nanocomposites in a direct way, and to use the compounds to achieve an efficient catalyst for hydrogen production. These nanocomposites, which were prepared by using the sol-gel supported gelatin fuel method, were analysed using XRD, FTIR and ESEM techniques. To determine the surface properties of these nanocomposites, the surface area and pore size were obtained. The measurements of optical absorption at the band gap were completed on UV-Vis spectrophotometer. Finally, the methanolysis reactions of $NaBH_4$ were performed using the $Cu_{2-x}Na_xO$/GO nanocomposite catalyst effect.

2. Experimental

Analar grades of copper nitrate trihydrate, sodium nitrate and gelatin powders were used for the preparation of $Cu_{2-x}Na_xO$/GO nanocomposites. The auto-combustion process was performed at 260 ^oC. The mass of gelatine is 50% of metal nitrates masses. The specific masses of metal nitrates were dissolved in 25 mL of distilled water separately. Thereafter, the solutions were added to the gelatin solution with continuous mixing for 120 min at a temperature of 80 ^oC. The precursor solution was then transferred to an electric oven operating at 260 ^oC. The evaporation of water started until the formation of a hydrogel. Finally, the auto-combustion process was started, and gases were released with the formation of nanocomposites.

One of the most important instruments for determining the crystalline structures and phase composition of materials is XRD. XRD pattern of the solid powder was analysed by Shimadzu

XRD 700 with $Cu_{K\alpha}$ radiation and wavelength of 1.54056 Å. The diffraction data were matched to the diffraction pattern from the Joint Committee on Powder Diffraction Standard (JCPDS) to identify the Miller indices and crystal structure. The main objective of investigating the FTIR spectrum is to detect chemical bondings and interactions inside the materials. Attenuated total reflection (ATR) spectroscopy was performed with Shimadzu spectrometer FTIR-100 Tracer with scanning spectra recorded in the range of 400 to 4000 cm^{-1}. The data of Raman spectra for the prepared nanostructures were recorded on a SENTERRA II Brucker Compact Raman Microscope. The laser wavelength was operated at 532 nm. The X-ray photoelectron spectroscopy (XPS) data of the catalysts were collected on (XPS; Thermo scientific K-alpha XPS spectrometer, Thermo Fisher Scientific, Waltham, USA). The source was a monochromic Al kα with a characteristic energy of 1486.6 eV. Scanning electron microscopy images were taken using a Thermofisher Quattro ESEM. Energy dispersive X-ray spectroscopy (EDX) was used in conjunction with ESEM to determine the elemental composition of the samples. The nitrogen isotherm loops for $Cu_{2-x}Na_xO$/GO nanocomposites were acquired from NOVA 4200e surface area and pore size analyzer. To release the trapped moisture molecules, the samples were degassed at 100 ^oC for 24 h. Thermo Scientific Evolution 300 UV-Vis spectrometer, which operates in the range of 200 to 1000 nm, was used to record the absorption spectra of nanocomposites. The powder of samples was dispersed in methanol via sonication for 30 min.

The hydrogen catalytic evaluation for the $Cu_{2-x}Na_xO$/GO nanocomposites was done at 293 K. The initial step includes mixing of 20 mg of the catalyst with 0.25 g of $NaBH_4$. Next, the mixture was inserted rapidly into a volumetric flask. Meanwhile, 10 mL of methanol was added to the mixture and the flask closed with glass stopper. At the same time, the stopwatch was started to record the time for the production of different volumes of hydrogen gas. The water displacement method was used to measure the volume of hydrogen gas.

3. Results and discussion

The XRD diffraction patterns of Cu_2O/GO, $Cu_{1.7}Na_{0.3}O$/GO and $Cu_{1.4}Na_{0.6}O$/GO shown in Fig. 1 clearly display strong peaks at scattering angles (2θ) values of 29.6°, 36.5°, 42.6°, 61.4°, 73.81° and 77.4°, which correspond to scattering from the crystal planes (110), (111), (200), (220), (311) and (222) of the face-centred cubic cuprous oxide, respectively, according to JCPDS card No.05-0667 [25]. The two additional peaks at 2θ =43.39 and 50.4 are evidence of the presence of metallic Cu [26]. The intensity of these two peaks decreased after the addition of sodium. Moreover, the peak located at 38.6^o with reflection (200) is assigned to CuO

orthorhombic crystal structure [27]. The average crystallite sizes of Cu_2O, $Cu_{1.7}Na_{0.3}O$ and $Cu_{1.4}Na_{0.6}O$ nanoparticles were determined using Debye–Scherrer formula [28-30] as given by equation 1.

$$D = \frac{0.9\lambda}{\beta cos\theta} \quad (1)$$

where D is the normal grain size of a crystallite, λ is the wavelength of X-ray and is equal to (1.5406 Å) for Cu $K\alpha_1$, and β is the full width at half maximum which can be obtained from the X-ray spectra. The average crystallite size of all samples was found to be 9 nm.

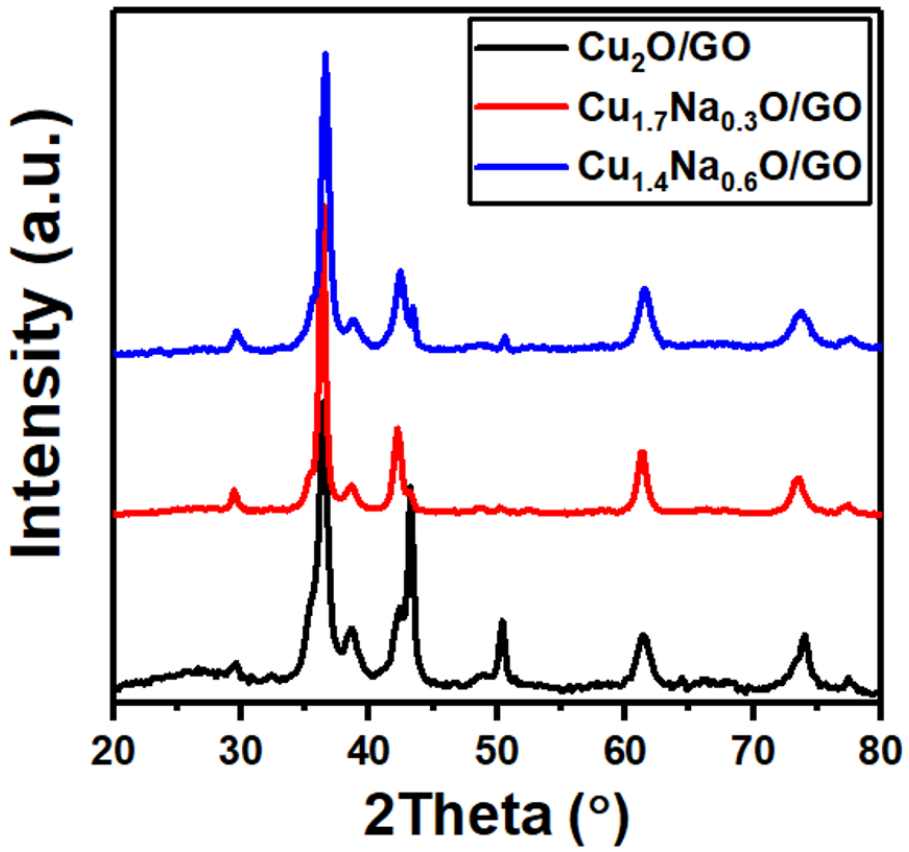

Fig. 1: XRD diffraction patterns of Cu_2O/GO, $Cu_{1.7}Na_{0.3}O$/GO and $Cu_{1.4}Na_{0.6}O$/GO nanostructures.

Fig.2 displays the transmittance (or absorption) as function of wavenumber of Cu_2O/GO, $Cu_{1.7}Na_{0.3}O$/GO, and $Cu_{1.4}Na_{0.6}O$/GO nanostructures as obtained by Fourier transform infrared spectroscopy (FTIR). The absorption bands at 484, 611, and 760 cm^{-1} are associated with the stretching vibration of the Cu–O in Cu_2O crystals [31]. The weak band absorption at 1128 cm^{-1} corresponds to C–C stretching vibration and O–H bending vibration [32]. The bands at 1314 and 1474 cm^{-1} weren't previously observed in the Cu_2O standard IR spectrum. Hence, these bands could be a result of the combustion of gelatin producing graphite oxide stretching [33].

Moreover, after adding Na^+ to Cu_2O, these two bands interfered resulting in a reduction in graphite oxides [34]. The intense peak at around 1395 cm^{-1} is assigned to the deformation vibration of the C-H band. The small band at around 2365 cm^{-1} is attributed to O=C=O stretching vibration [35]. The broad absorption band between 2505 cm^{-1} and 3655 cm^{-1} correlates to hydroxyl (OH) functional groups [36]. For the samples $Cu_{1.7}Na_{0.3}O$/GO and $Cu_{1.4}Na_{0.6}O$/GO, two absorption bands located at 835 and 879 cm^{-1} are observed that comes due to stretching vibrations of Na–Cu–O as reported in the literature [37].

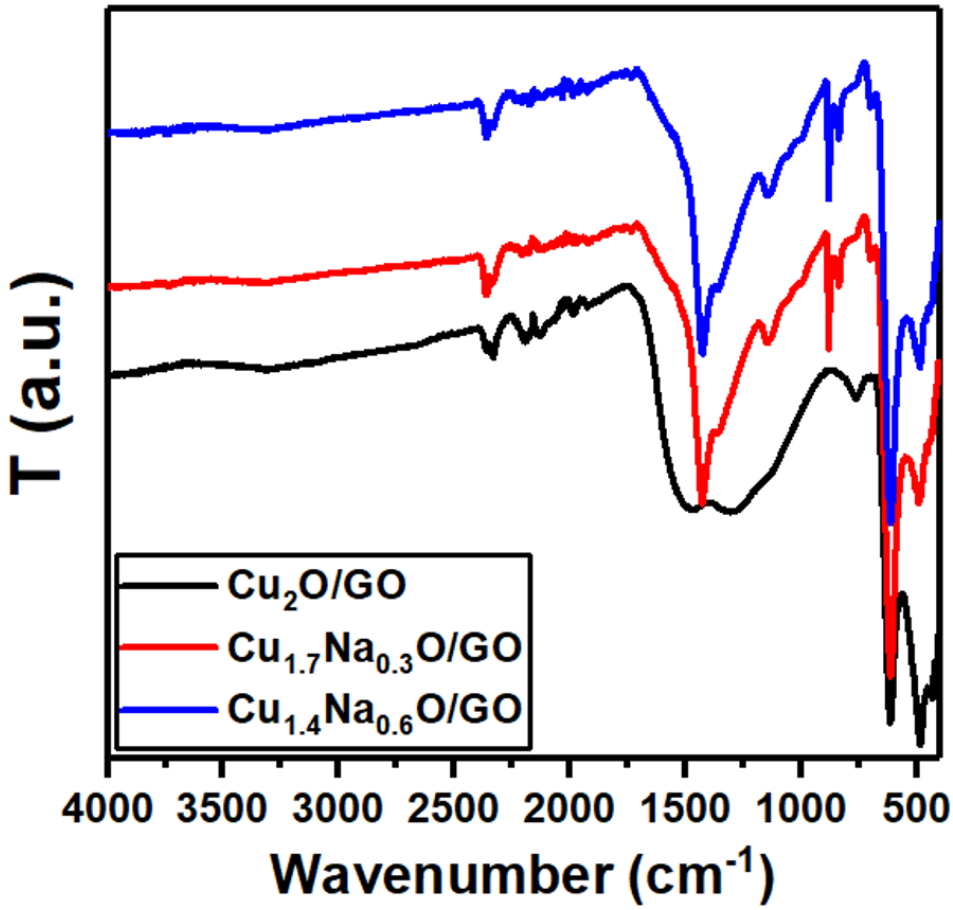

Fig. 2: FTIR spectra of Cu_2O/GO, $Cu_{1.7}Na_{0.3}O$/GO and $Cu_{1.4}Na_{0.6}O$/GO nanostructures.

The hydroxyl and carboxyl groups produce negatively charged GO. During the growth process, positively charged copper ions would then interact with negatively charged GO. The electrostatic interaction generates these attractions. The procedure continued with the growth

of Cu_2O nanoparticles on the two-dimensional GO nanosheets during the combustion process. After the inclusion of sodium, the GO nanosheets become reduced to thick layers.

A common approach for describing the structural and other crucial characteristics of graphene, such as disorder and defect structures, is Raman spectroscopy. The data of Raman spectra of the $Cu_{2-x}Na_xO$/GO nanostructures are plotted in Fig. 3. The band observed at 622 cm-1 is assigned to the infrared allowed mode $\Gamma^{(2)}_{15-}$ (TO) for Cu_2O [38]. The D band of GO is detected at 1300 cm^{-1} [39]. The increase of sodium content (0.3-0.6) resulted in a shift to lower wavenumber of 1154 cm^{-1}. Therefore, the GO sheets are reduced as explained in the literature [40]. Moreover, the position of 2D band of GO is observed at 2805 cm^{-1} [41] and shifted to 2751 cm^{-1} at 0.6% of sodium content. All these findings confirm the reduction of GO after the addition of sodium. The strong band located at 2030 cm^{-1} comes due to carbonyl and carboxylic groups have a C=O stretching vibration [42]. Further, this band recognize the formation of GO sheets.

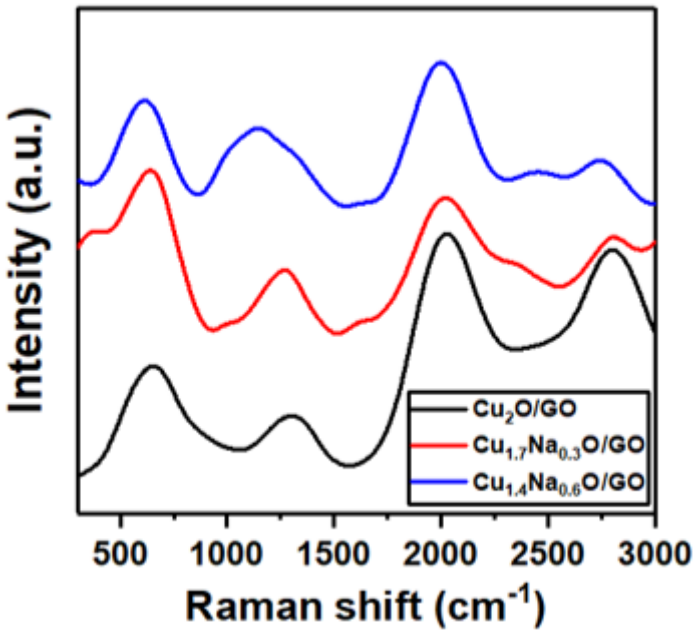

Fig. 3 Raman spectra of Cu_2O/GO, $Cu_{1.7}Na_{0.3}O$/GO and $Cu_{1.4}Na_{0.6}O$/GO nanostructures.

The XPS method was used to investigate the specific surface composition of $Cu_{2-x}Na_xO$/GO nanostructures. The wide-range XPS spectra of the Cu_2O/GO, $Cu_{1.7}Na_{0.3}O$/GO and $Cu_{1.4}Na_{0.6}O$/GO samples are depicted in Fig. 4 and reveals Cu 2p, O 1s, C 1s, Cu 3s, and Na 1s. The peak of C 1s located at 287.08 eV is assigned to C=O and thus confirm the formation of GO in all the samples. This peak shifted to 289.08 at 0.6% of sodium content and thus indicate that graphene oxide was reduced to rGO [43]. Between 570 and 721 eV, an Auger Cu

LMM triplet was found, which indicates energy levels of the Cu Auger process. These Auger peaks correspond to Cu_2O [44]. For the samples $Cu_{1.7}Na_{0.3}O$/GO and $Cu_{1.4}Na_{0.6}O$/GO the Na 1s peak was observed at 1075.08 eV that confirm the presence of sodium content [45]. Moreover, an Auger peak for Na was detected at 500.08 eV that agree with the literature [46].

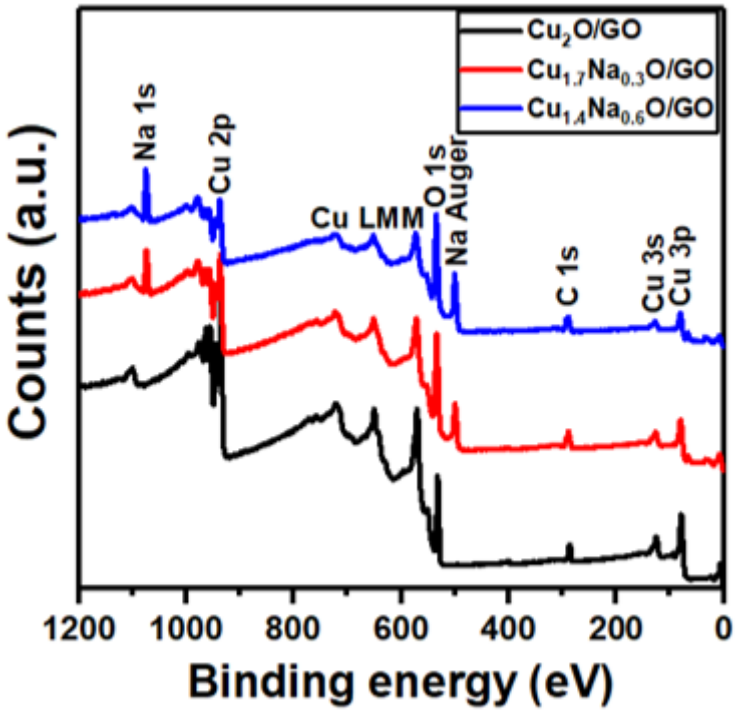

Fig. 4 XPS survey spectra of $Cu_{2-x}Na_xO$/GO nanostructures

The high-resolution Cu 2p spectra for all the samples are shown in Fig. 5a. Two main peaks, Cu $2p^{3/2}$ and Cu $2p^{1/2}$, as well as two satellite peaks can be seen in all the Cu 2p spectra. The positions of Cu $2p^{3/2}$ and Cu $2p^{1/2}$ peaks are 935.78 and 955.48 eV for the Cu_2O/GO sample. After the addition of 0.6% sodium content, the positions of these two peaks shifted to 938.08 and 957.88 eV. These peaks correspond to the Cu^{2+} state (CuO) [47]. The binding energy separation between these two peaks is 19.7 eV. The presence of an empty Cu 3d shell corresponding to Cu(II) species at the Cu_2O surface is confirmed by satellite peaks with binding energies of 943.88 and 968.32 eV [48]. The high-resolution peaks of O 1s for all the samples are shown in Fig. 5b. The binding energies at 532.08 and 535.08 eV in the O 1 s spectra were ascribed to dissociated oxygen species and OH groups [49].

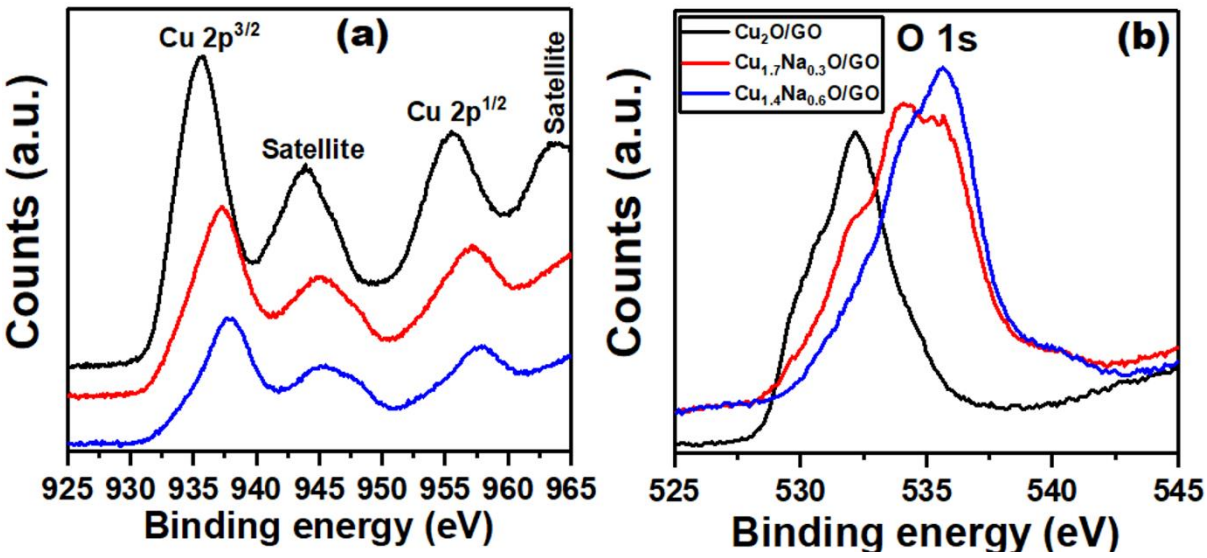

Fig. 5 XPS plots of (a) Cu 2p and (b) O 1s for $Cu_{2-x}Na_xO$/GO nanostructures

A high-resolution environmental scanning electron microscope (ESEM) was used to examine the surface characteristics and morphology of $Cu_{2-x}Na_xO$/GO nanostructures. The ESEM images of Cu_2O/GO, $Cu_{1.7}Na_{0.3}O$/GO and $Cu_{1.4}Na_{0.6}O$/GO nanocomposites are shown in Fig. 6 (a-c). On a large scale, these images clearly reveal that nanoscale $Cu_{2-x}Na_xO$ crystals are evenly integrated into GO. Moreover, the increase of sodium content allowed reducing GO to form two-dimensional (2D) stack layers. This result indicates a decrease of the surface area as the percentage of sodium increases. Energy dispersive X-ray spectroscopy (EDX) was used to determine the elemental composition of $Cu_{1.4}Na_{0.6}O$/GO nanocomposite as shown in Fig. 6 (d). The stoichiometric ratios of copper, oxygen, sodium and carbon are shown in the inset of Fig. 6 (d). Moreover, the EDX data of individual elements are listed in Table 1 and confirm the presence of all the elements of the $Cu_{2-x}Na_xO$/GO nanostructures.

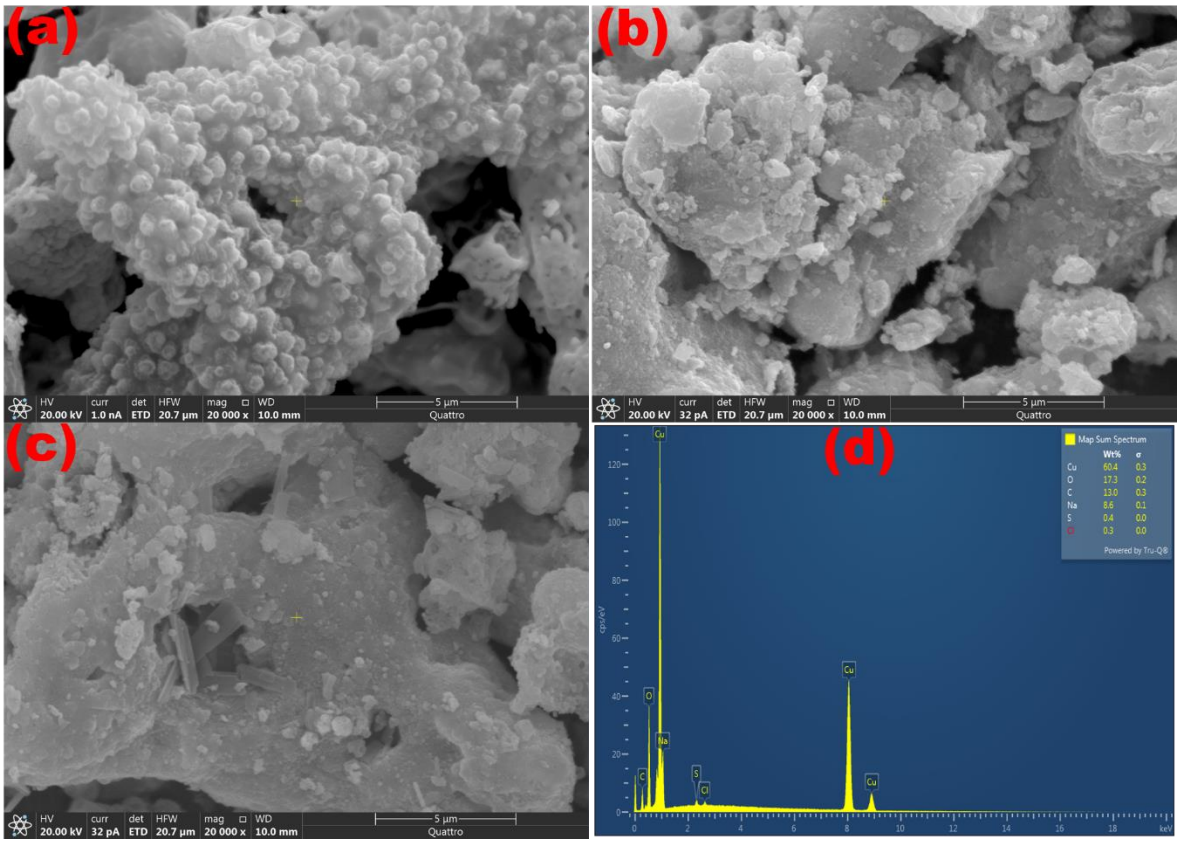

Fig. 6: ESEM scans of (a) Cu_2O/GO, (b) $Cu_{1.7}Na_{0.3}O$/GO, (c) $Cu_{1.4}Na_{0.6}O$/GO and (d) EDX data for $Cu_{1.4}Na_{0.6}O$/GO nanostructures.

Table 1 Weight % obtained from EDX analysis of elements present at the surface of $Cu_{2-x}Na_xO$/GO nanostructures

Sample	Cu (wt%)	O (wt%)	Na (wt%)	C (wt%)
Cu_2O/GO	50.3	14.5	-	34.5
$Cu_{1.7}Na_{0.3}O$/GO	55.4	16.6	4.2	23.4
$Cu_{1.4}Na_{0.6}O$/GO	60.4	17.3	8.6	13.0

Fig. 7 (a) depicts the BET surface area analyses for Cu_2O/GO, $Cu_{1.7}Na_{0.3}O$/GO and $Cu_{1.4}Na_{0.6}O$/GO nanocomposites based on low temperature nitrogen adsorption isotherm. The $Cu_{2-x}Na_xO$/GO nanocomposites produced demonstrate a characteristic hysteresis loop that may be attributed to type-IV isotherm. The values of BET surface area are 122, 63 and 59 m^2/g for Cu_2O/GO, $Cu_{1.7}Na_{0.3}O$/GO and $Cu_{1.4}Na_{0.6}O$/GO nanocomposites, respectively. The incorporation of sodium into Cu_2O/GO nanocomposite reduced the surface area of the samples.

The BJH data showed pore size values of 2.32, 1.76 and 1.88 nm for Cu_2O/GO, $Cu_{1.7}Na_{0.3}O$/GO and $Cu_{1.4}Na_{0.6}O$/GO nanocomposites, respectively. The prepared samples showed a porous structure as a result of releasing gases during the combustion process [50]. Broad mesopores spread between 4 and 8 nm, which provide more active sites, are seen to display hierarchical pore structure in the pore size distribution (Fig. 7 (b)).

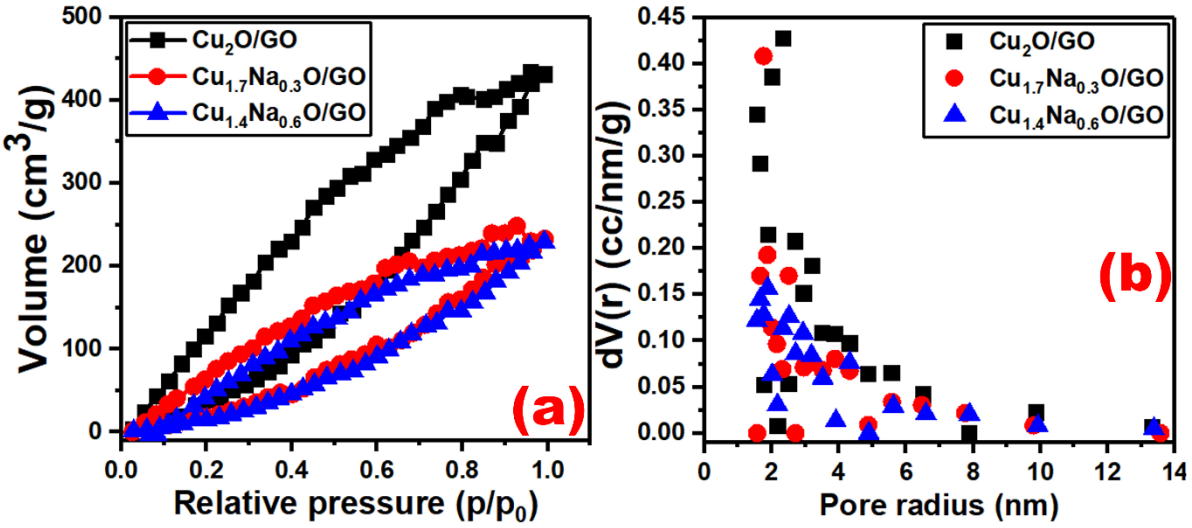

Fig. 7: Plots (a) nitrogen isotherms and (b) pore size distribution data of Cu_2O/GO, $Cu_{1.7}Na_{0.3}O$/GO and $Cu_{1.4}Na_{0.6}O$/GO nanostructures.

One of the key characteristics that is crucial to understanding the energy structures and uses of photocatalysis is the performance of optical absorption. A UV-Vis spectrometer was used to evaluate the absorption spectra of Cu_2O/GO, $Cu_{1.7}Na_{0.3}O$/GO and $Cu_{1.4}Na_{0.6}O$/GO nanocomposites as shown Fig. 8 (a). The spectra of nanocomposites showed a redshift of the optical absorption edge with increasing the content of sodium. The broad absorption band around 450 nm is assigned to the intrinsic bandgap absorption [51]. Therefore, the optical energy bandgaps (E_g) could be estimated from the Tauc method as expressed by equation 2 for direct allowed transitions [52-54].

$$\alpha h\upsilon = B(h\upsilon - E_g)^{0.5} \qquad (2)$$

where α is the absorption coefficient, h represents Plank's constant, ν is the frequency of incident light and B is a constant. The Tauc plots of $(\alpha h\nu)^2$ versus photon energy (hν) of the nanocomposites are shown in Fig. 8(b). The extrapolation of straight lines at $(\alpha h\nu)^2 = 0$ determine the values of E_g. The corresponding energy bandgaps are 2.14 eV, 2.0 eV and 1.72 eV for Cu_2O/GO, $Cu_{1.7}Na_{0.3}O$/GO and $Cu_{1.4}Na_{0.6}O$/GO nanocomposites, respectively. The

decrease of the optical energy bandgap is due to the formation of new energy levels in the forbidden bandgap [55].

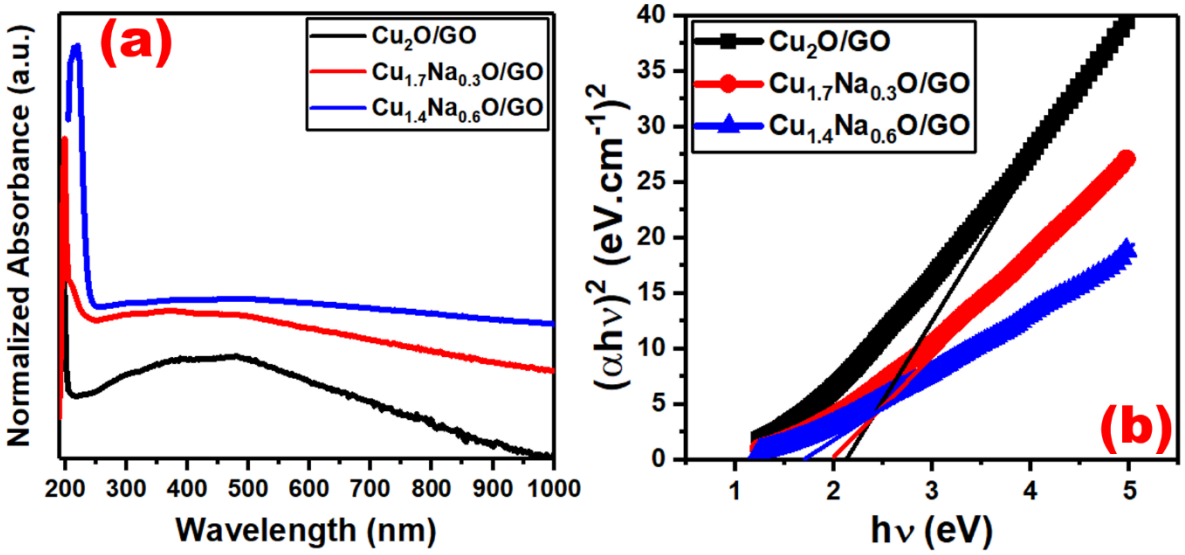

Fig. 8: Plots (a) absorbance against wavelength and (b) $(\alpha h\nu)^2$ versus photon energy for Cu_2O/GO, $Cu_{1.7}Na_{0.3}O$/GO and $Cu_{1.4}Na_{0.6}O$/GO nanostructures.

$Cu_{1-x}Na_xO$/GO nanocomposites are thought to be an effective catalyst for hydrogen generation from sodium borohydride ($NaBH_4$). The self-hydrolysis of $NaBH_4$ produces stable solutions that evolve limited amounts of hydrogen. In comparison to water, methanol is a light alcohol and possesses high reactivity for $NaBH_4$ hydrolysis to produce H_2 gas. Furthermore, methanol reduces the temperature of the reaction and thus produces hydrogen at lower temperatures [56]. The observations of hydrogen evolution from $NaBH_4$-methanolysis process are shown in Fig. 9. The results show that $Cu_{1.4}Na_{0.6}O$/GO nanocomposite sample presents the fastest rate of hydrogen production.

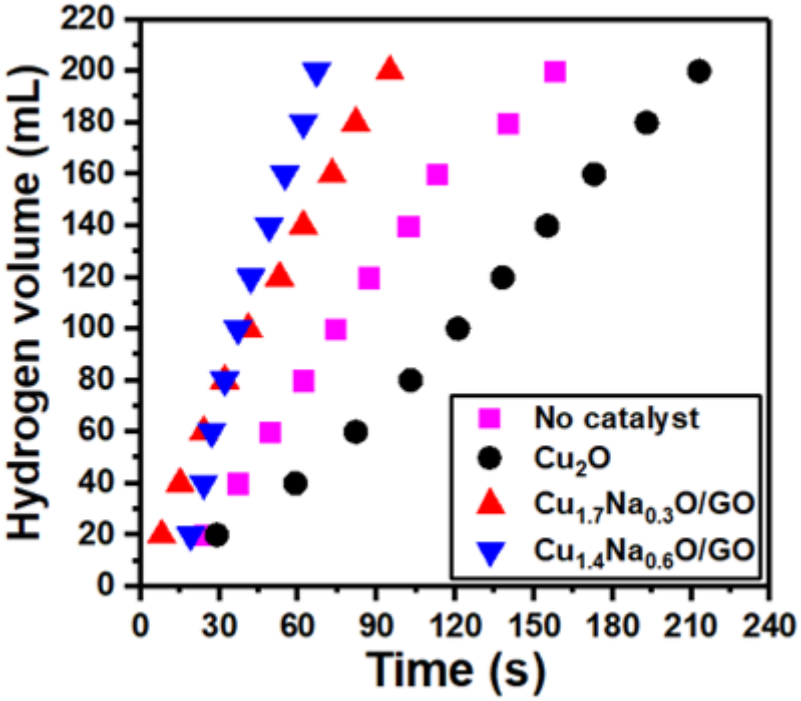

Fig. 9: Hydrogen catalytic performance of Cu_2O/GO, $Cu_{1.7}Na_{0.3}O$/GO and $Cu_{1.4}Na_{0.6}O$/GO nanostructures.

The self-hydrolysis of $NaBH_4$ in methanol produces Na^+ and BH_4^- ions. The active sites on the surface of the catalyst adsorb BH_4^- ions. Therefore, the catalyst with more active sites is expected to accelerate the hydrogen evolution. Other elements that influence the activity of a catalyst include particle size and degree of dispersion. When a catalyst has a small particle size and high dispersion, the interaction with $NaBH_4$ will be improved. The efficient catalyst adsorbs more BH_4^- ions in a shorter period, resulting in greater hydrogen production [**57**].

The effectiveness of the catalyst to speed up the reaction is strongly influenced by the rate of hydrogen generation (k). The values of k can be determined using equation 3 [58-60].

$$k = \frac{V}{t.m_{cat}} \qquad (3)$$

where V is the volume of H_2 gas, t is time and m_{cat} represents the mass of the catalyst. The slopes of H_2 volume versus time plotted in Fig. 9 were used to calculate the rate of hydrogen generation. Values of 3055, 6167 and 10981 mL/g.min were obtained for Cu_2O/GO, $Cu_{1.7}Na_{0.3}O$/GO and $Cu_{1.4}Na_{0.6}O$/GO nanocomposite samples, respectively. Fig. 10 summarises the hydrogen production rates of all nanocomposites investigated in this work.

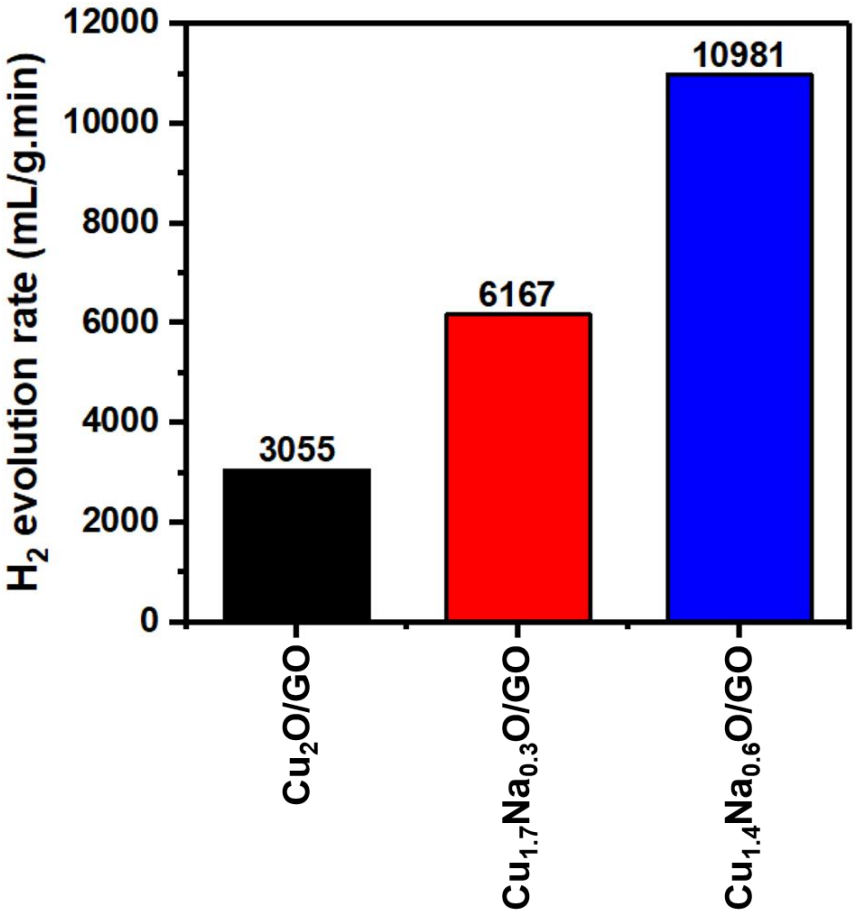

Fig. 10: Hydrogen production rates of Cu_2O/GO, $Cu_{1.7}Na_{0.3}O$/GO and $Cu_{1.4}Na_{0.6}O$/GO nanocomposites.

Interestingly, the rate of hydrogen generation was improved upon the increase of Na content. $Cu_{1.4}Na_{0.6}O$/GO sample showed the highest hydrogen production rate. The porous surface structure of the nanocomposites achieved more active sites and thus attracted more BH_4^- ions. Moreover, the decrease of pore size limits the adsorption of H_2 gas and thus improves the rate of hydrogen production. Furthermore, Na reacts with the metal oxide catalyst to form Na_2O, which has a higher basicity than the original metal oxide catalyst. This increased basicity can enhance the hydrolysis reaction of $NaBH_4$.

The data of hydrogen generation rates of Cu_2O/GO, $Cu_{1.7}Na_{0.3}O$/GO and $Cu_{1.4}Na_{0.6}O$/GO nanocomposites are superior to those reported values in the literature. The rate of generation for $Cu_{1.4}Na_{0.6}O$/GO is higher than that of NiS-g-C_3N_4 nanosheets (8654 mL/g.min) [57]. Moreover, the generation rates achieved in the current study are higher than those of Ru/NiO-Ni foam (6000 mL/g.min) [61], Ru_5Co/C (9360 mL/g.min) [62] and Ni_2P (3700 mL/g.min)

[63]. These findings evidence that Cu_2O/GO, $Cu_{1.7}Na_{0.3}O$/GO and $Cu_{1.4}Na_{0.6}O$/GO nanocomposites are more efficient for hydrogen catalytic production from $NaBH_4$.

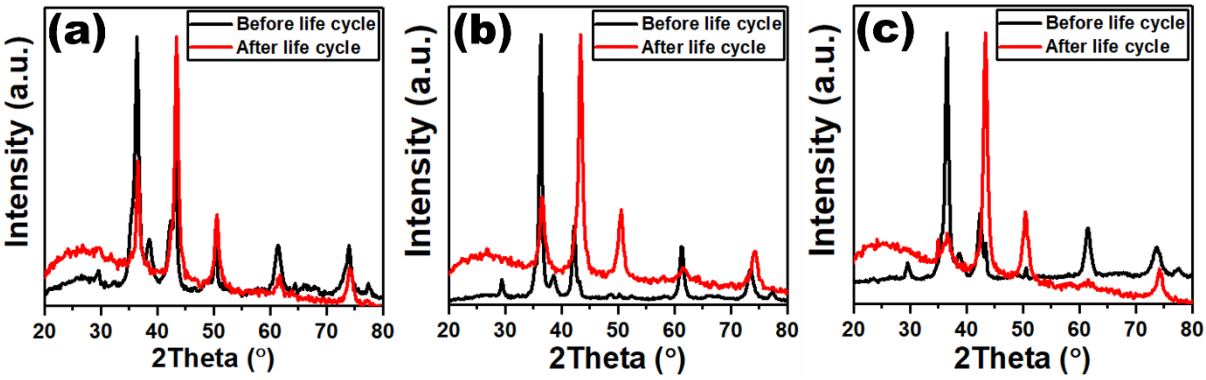

Fig. 11 XRD patterns of (a) Cu_2O/GO, (b) $Cu_{1.7}Na_{0.3}O$/GO and (c) $Cu_{1.4}Na_{0.6}O$/GO catalysts before and after life cycle

The XRD spectra of the Cu_2O/GO, $Cu_{1.7}Na_{0.3}O$/GO and $Cu_{1.4}Na_{0.6}O$/GO catalysts before and after life cycle were plotted in Fig. 11. The data of XRD showed the catalysts have robust structure and can be applied to hydrogen production catalysis for many times.

Conclusions

Cu_2O/GO, $Cu_{1.7}Na_{0.3}O$/GO and $Cu_{1.4}Na_{0.6}O$/GO nanocomposite catalysts were fabricated by auto-combustion technique. The XRD scans showed that all samples have a cubic crystal structure. The FTIR spectra analysis revealed the formation of $Cu_{1-x}Na_xO$/GO nanocomposites. ESEM images provided evidence that nanoscale $Cu_{2-x}Na_xO$ crystals were integrated into the GO nanosheets. The values of BET surface areas were 122, 63 and 59 m^2/g for Cu_2O/GO, $Cu_{1.7}Na_{0.3}O$/GO and $Cu_{1.4}Na_{0.6}O$/GO nanocomposites, respectively. The optical energy bandgaps were found to be 2.14, 2.0 and 1.72 eV for Cu_2O/GO, $Cu_{1.7}Na_{0.3}O$/GO and $Cu_{1.4}Na_{0.6}O$/GO nanocomposites, respectively. The hydrogen catalytic production from $NaBH_4$ was improved upon the addition of sodium into Cu_2O/GO. The maximum rate of hydrogen generation was 10981 mL/g.min for the $Cu_{1.4}Na_{0.6}O$/GO nanocomposite sample.

References

1. Akal, D., Öztuna, S., & Büyükakın, M. K. (2020). A review of hydrogen usage in internal combustion engines (gasoline-Lpg-diesel) from combustion performance aspect. International journal of hydrogen energy, 45(60), 35257-35268.
2. Anil, S., Indraja, S., Singh, R., Appari, S., & Roy, B. (2022). A review on ethanol steam reforming for hydrogen production over Ni/Al_2O_3 and Ni/CeO_2 based catalyst powders. International Journal of Hydrogen Energy.
3. Wang, T., Jiang, T., Zhang, H., & Zhao, Y. (2022). Advances in catalysts for hydrogen production by methanolysis of sodium borohydride. International Journal of Hydrogen Energy.
4. Xu, X., Zhou, Q., & Yu, D. (2022). The future of hydrogen energy: Bio-hydrogen production technology. International Journal of Hydrogen Energy.
5. Yang, G. C., Pan, Q. Y., Yang, P., Liu, Y. S., Du, Y., & Wang, K. (2022). Heteropolyacids supported on hierarchically macro/mesoporous TiO_2: efficient catalyst for deep oxidative desulfurization of fuel. Tungsten, 1-10.
6. Mallakpour, S., & Khadem, E. (2016). Carbon nanotube–metal oxide nanocomposites: Fabrication, properties and applications. Chemical Engineering Journal, 302, 344-367.
7. Yu, T., Li, S., Zhang, L., Li, F., Wang, J., Pan, H., & Zhang, D. (2023). In situ growth of ZIF-67-derived nickel-cobalt-manganese hydroxides on 2D V_2CTx MXene for dual-functional orientation as high-performance asymmetric supercapacitor and electrochemical hydroquinone sensor. Journal of Colloid and Interface Science, 629, 546-558.
8. Ajala, O. J., Tijani, J. O., Bankole, M. T., & Abdulkareem, A. S. (2022). A critical review on graphene oxide nanostructured material: Properties, Synthesis, characterization and application in water and wastewater treatment. Environmental Nanotechnology, Monitoring & Management, 18, 100673.
9. Lingamdinne, L. P., Koduru, J. R., & Karri, R. R. (2019). A comprehensive review of applications of magnetic graphene oxide based nanocomposites for sustainable water purification. Journal of environmental management, 231, 622-634.
10. Li, X., Shen, R., Ma, S., Chen, X., & Xie, J. (2018). Graphene-based heterojunction photocatalysts. Applied Surface Science, 430, 53-107.
11. Kumar, R., Sahoo, S., Joanni, E., Singh, R. K., Yadav, R. M., Verma, R. K., ... & Matsuda, A. (2019). A review on synthesis of graphene, h-BN and MoS 2 for energy storage applications: Recent progress and perspectives. Nano research, 12, 2655-2694.
12. Lingamdinne, L. P., Koduru, J. R., & Karri, R. R. (2019). A comprehensive review of applications of magnetic graphene oxide based nanocomposites for sustainable water purification. Journal of environmental management, 231, 622-634.
13. Pan, J., Li, S., Zhang, L., Yu, T., Li, F., Zhang, W., ... & Li, X. (2022). Reduced graphene oxide/Ni foam supported ZIF-67 derived $CuCo_2S_4@CoS_2$ core-shell heterostructure for boosted electrochemical energy storage. Journal of Energy Storage, 47, 103550.
14. Kaur, G., Dewasi, A., Mitra, A., & Yadav, K. L. (2016). Effect of Nitrogen Gas Annealing on the Properties of Pulsed Laser Deposited Cu_2O Thin Films. Advanced Science Letters, 22(4), 905-910.

15. Guo, D., Wang, L., Du, Y., Ma, Z., & Shen, L. (2015). Preparation of octahedral Cu2O nanoparticles by a green route. Materials Letters, 160, 541-543.
16. Zhang, Z., Sun, L., Wu, Z., Liu, Y., & Li, S. (2020). Facile hydrothermal synthesis of CuO–Cu_2O/GO nanocomposites for the photocatalytic degradation of organic dye and tetracycline pollutants. New Journal of Chemistry, 44(16), 6420-6427.
17. Feng, Y., Wang, R., Yin, J., Zhan, F., Chen, K., Jiao, T., ... & Peng, Q. (2020). Facile synthesis of Cu_2O nanoparticle-loaded carbon nanotubes composite catalysts for reduction of 4-nitrophenol. Current Nanoscience, 16(4), 617-624.
18. Duman, F., Atelge, M. R., Kaya, M., Atabani, A. E., Kumar, G., Sahin, U., & Unalan, S. (2020). A novel Microcystis aeruginosa supported manganese catalyst for hydrogen generation through methanolysis of sodium borohydride. International Journal of Hydrogen Energy, 45(23), 12755-12765.
19. Dönmez, F., & Ayas, N. (2021). Synthesis of Ni/TiO_2 catalyst by sol-gel method for hydrogen production from sodium borohydride. International Journal of Hydrogen Energy, 46(57), 29314-29322.
20. Tomboc, G. R. M., Tamboli, A. H., & Kim, H. (2017). Synthesis of Co_3O_4 macrocubes catalyst using novel chitosan/urea template for hydrogen generation from sodium borohydride. Energy, 121, 238-245.
21. Durano, M. M., Tamboli, A. H., & Kim, H. (2017). Cobalt oxide synthesized using urea precipitation method as catalyst for the hydrolysis of sodium borohydride. Colloids and Surfaces A: Physicochemical and Engineering Aspects, 520, 355-360.
22. Groven, L. J., Pfeil, T. L., & Pourpoint, T. L. (2013). Solution combustion synthesized cobalt oxide catalyst precursor for NaBH4 hydrolysis. International journal of hydrogen energy, 38(15), 6377-6380.
23. Prasad, D., Patil, K. N., Sandhya, N., Chaitra, C. R., Bhanushali, J. T., Samal, A. K., ... & Nagaraja, B. M. (2019). Highly efficient hydrogen production by hydrolysis of NaBH4 using eminently competent recyclable Fe_2O_3 decorated oxidized MWCNTs robust catalyst. Applied Surface Science, 489, 538-551.
24. Patil, K. N., Prasad, D., Manoorkar, V. K., Nabgan, W., Nagaraja, B. M., & Jadhav, A. H. (2021). Engineered nano-foam of tri-metallic (FeCuCo) oxide catalyst for enhanced hydrogen generation via $NaBH_4$ hydrolysis. Chemosphere, 281, 130988.
25. Li, B., Li, Y., Zhao, Y., & Sun, L. (2013). Shape-controlled synthesis of Cu_2O nano/microcrystals and their antibacterial activity. Journal of Physics and Chemistry of Solids, 74(12), 1842-1847.
26. Karimzadeh, M., Niknam, K., Manouchehri, N., & Tarokh, D. (2018). A green route for the cross-coupling of azide anions with aryl halides under both base and ligand-free conditions: Exceptional performance of a Cu_2O–CuO–Cu–C nanocomposite. RSC advances, 8(45), 25785-25793.
27. Raul, P. K., Senapati, S., Sahoo, A. K., Umlong, I. M., Devi, R. R., Thakur, A. J., & Veer, V. (2014). CuO nanorods: a potential and efficient adsorbent in water purification. Rsc Advances, 4(76), 40580-40587.
28. Alshammari, A. H., Alshammari, M., Alhassan, S., Alshammari, K., Alotaibi, T., & Taha, T. A. M. (2023). MoO_3/S@g-C_3N_4 Nanocomposite Structures: Synthesis, Characterization, and Hydrogen Catalytic Performance. Nanomaterials, 13(5), 820.

29. Abdullah, M., Ansari, M. Z., Ahamd, Z., John, P., Manzoor, S., Shawky, A. M., ... & Taha, T. A. (2023). Ag_2Se/SnTe nanorod as potential candidate for energy conversion system developed via hydrothermal route. Ceramics International, 49(4), 6780-6789.
30. Alshammari, A. H., Alshammari, M., Ibrahim, M., Alshammari, K., & Taha, T. A. M. (2023). New Hybrid PVC/PVP Polymer Blend Modified with Er_2O_3 Nanoparticles for Optoelectronic Applications. Polymers, 15(3), 684.
31. Karimzadeh, M., Niknam, K., Manouchehri, N., & Tarokh, D. (2018). A green route for the cross-coupling of azide anions with aryl halides under both base and ligand-free conditions: Exceptional performance of a Cu_2O–CuO–Cu–C nanocomposite. RSC advances, 8(45), 25785-25793.
32. Xu, C., Wang, X., Yang, L., & Wu, Y. (2009). Fabrication of a graphene–cuprous oxide composite. Journal of Solid State Chemistry, 182(9), 2486-2490.
33. Xu, C., Wang, X., Yang, L., & Wu, Y. (2009). Fabrication of a graphene–cuprous oxide composite. Journal of Solid State Chemistry, 182(9), 2486-2490.
34. Emiru, T. F., & Ayele, D. W. (2017). Controlled synthesis, characterization and reduction of graphene oxide: A convenient method for large scale production. Egyptian Journal of Basic and Applied Sciences, 4(1), 74-79.
35. Sundar, S., Venkatachalam, G., & Kwon, S. J. (2018). Biosynthesis of copper oxide (CuO) nanowires and their use for the electrochemical sensing of dopamine. Nanomaterials, 8(10), 823.
36. Sudha, V., Murugadoss, G., & Thangamuthu, R. (2021). Structural and morphological tuning of Cu-based metal oxide nanoparticles by a facile chemical method and highly electrochemical sensing of sulphite. Scientific Reports, 11(1), 3413.
37. Siddiqui, H., Parra, M. R., Qureshi, M. S., Malik, M. M., & Haque, F. Z. (2018). Studies of structural, optical, and electrical properties associated with defects in sodium-doped copper oxide (CuO/Na) nanostructures. Journal of materials science, 53(12), 8826-8843.
38. Powell, D., Compaan, A., Macdonald, J. R., & Forman, R. A. (1975). Raman-scattering study of ion-implantation-produced damage in Cu 2 O. Physical Review B, 12(1), 20.
39. Claramunt, S., Varea, A., Lopez-Diaz, D., Velázquez, M. M., Cornet, A., & Cirera, A. (2015). The importance of interbands on the interpretation of the Raman spectrum of graphene oxide. The Journal of Physical Chemistry C, 119(18), 10123-10129.
40. Muzyka, R., Drewniak, S., Pustelny, T., Chrubasik, M., & Gryglewicz, G. (2018). Characterization of graphite oxide and reduced graphene oxide obtained from different graphite precursors and oxidized by different methods using Raman spectroscopy. Materials, 11(7), 1050.
41. Lopez-Diaz, D., Delgado-Notario, J. A., Clerico, V., Diez, E., Merchan, M. D., & Velázquez, M. M. (2020). Towards understanding the Raman spectrum of graphene oxide: the effect of the chemical composition. Coatings, 10(6), 524.
42. Rajasekar, P., Rao, G., Kumar, A. S., Prakash, J., Rathinasabapathi, P., & Venkatasubbu, G. D. (2023). Interaction of BSA with graphene oxide: Influence on the bioactivity of graphene oxide. Diamond and Related Materials, 132, 109629.
43. Kasturi, S., Torati, S. R., Eom, Y. J., Ahmad, S., Lee, B. J., Yu, J. S., & Kim, C. (2020). Real-time monitored photocatalytic activity and electrochemical performance of an

rGO/Pt nanocomposite synthesized via a green approach. RSC advances, 10(23), 13722-13731.
44. Platzman, I., Brener, R., Haick, H., & Tannenbaum, R. (2008). Oxidation of polycrystalline copper thin films at ambient conditions. The Journal of Physical Chemistry C, 112(4), 1101-1108.
45. Mekki, A., Holland, D., McConville, C. F., & Salim, M. (1996). An XPS study of iron sodium silicate glass surfaces. Journal of non-crystalline solids, 208(3), 267-276.
46. Miura, Y., Kusano, H., Nanba, T., & Matsumoto, S. (2001). X-ray photoelectron spectroscopy of sodium borosilicate glasses. Journal of non-crystalline solids, 290(1), 1-14.
47. Bayat, F., & Sheibani, S. (2022). Enhancement of photocatalytic activity of CuO-Cu_2O heterostructures through the controlled content of Cu_2O. Materials Research Bulletin, 145, 111561.
48. Aguirre, M. E., Zhou, R., Eugene, A. J., Guzman, M. I., & Grela, M. A. (2017). Cu_2O/TiO_2 heterostructures for CO_2 reduction through a direct Z-scheme: Protecting Cu_2O from photocorrosion. Applied Catalysis B: Environmental, 217, 485-493.
49. Saeed, H., Ikram, M., Haider, A., Naz, S., Ul-Hamid, A., Nabgan, W., ... & Khan, S. (2023). Efficient dye degradation in the presence of reducing agent and bactericidal behavior with in silico molecular docking of z-scheme $P_3HT/g\text{-}C_3N_4$ doped CuO heterojunction. Surfaces and Interfaces, 38, 102804.
50. Xu, C., Manukyan, K. V., Adams, R. A., Pol, V. G., Chen, P., & Varma, A. (2019). One-step solution combustion synthesis of CuO/Cu_2O/C anode for long cycle life Li-ion batteries. Carbon, 142, 51-59.
51. Yu, Y., Zhang, L., Wang, J., Yang, Z., Long, M., Hu, N., & Zhang, Y. (2012). Preparation of hollow porous Cu2O microspheres and photocatalytic activity under visible light irradiation. Nanoscale Research Letters, 7, 1-6.
52. Alshammari, A. H., Alshammari, K., Alshammari, M., & Taha, T. A. M. (2023). Structural and Optical Characterization of g-C3N4 Nanosheet Integrated PVC/PVP Polymer Nanocomposites. Polymers, 15(4), 871.
53. Ahmed, R. M., Taha, T. A., & Ezz-Eldin, F. M. (2021). Investigation of Sm2O3 effect on opto-electrical parameters and dielectric properties of some fluorophosphate glasses. Journal of Materials Science: Materials in Electronics, 32, 28919-28934.
54. Ahmed, R. M., Atta, M. M., & Taha, E. O. (2021). Optical spectroscopy, thermal analysis, and dynamic mechanical properties of graphene nano-platelets reinforced polyvinylchloride. Journal of Materials Science: Materials in Electronics, 32(17), 22699-22717.
55. Wang, X., Gong, J., Dong, Y., An, S., Zhang, X., & Tian, J. (2022). Energy band engineering of hydroxyethyl group grafted on the edge of 3D $g\text{-}C_3N_4$ nanotubes for enhanced photocatalytic H2 production. Materials Today Physics, 27, 100806.
56. Fernandes, V. R., Pinto, A. M. F. R., & Rangel, C. M. (2010). Hydrogen production from sodium borohydride in methanol–water mixtures. International journal of hydrogen energy, 35(18), 9862-9868.
57. Alshammari, A. H., Alshammari, K., Alotaibi, T., Alshammari, M., Alhassan, S., & Taha, T. A. M. (2023). In Situ Polycondensation Synthesis of $NiS\text{-}g\text{-}C_3N_4$

Nanocomposites for Catalytic Hydrogen Generation from NaBH4. Nanomaterials, 13(5), 938.
58. Saka, C. (2022). Phosphorus decorated g-C_3N_4-TiO_2 particles as efficient metal-free catalysts for hydrogen release by NaBH4 methanolysis. Fuel, 322, 124196.
59. Saka, C. (2022). g-C_3N_4 particles with boron and oxygen dopants/carbon vacancies for efficient dehydrogenation in sodium borohydride methanolysis. International Journal of Hydrogen Energy, 47(44), 19016-19026.
60. Patel, N., Fernandes, R., & Miotello, A. (2009). Hydrogen generation by hydrolysis of NaBH4 with efficient Co–P–B catalyst: a kinetic study. Journal of Power Sources, 188(2), 411-420.
61. Wang, F., Luo, Y., Zhang, Y., Wang, Y., & Zhu, H. (2020). Preparation of bush-like Ru/NiO-Ni foam catalyst and its performance in hydrogen production from sodium borohydride alcoholysis. Energy & Fuels, 34(9), 11365-11372.
62. Wang, F., Wang, Y., Zhang, Y., Luo, Y., & Zhu, H. (2018). Highly dispersed RuCo bimetallic nanoparticles supported on carbon black: enhanced catalytic activity for hydrogen generation from NaBH4 methanolysis. Journal of materials science, 53(9), 6831-6841.
63. Yan, K., Li, Y., Zhang, X., Yang, X., Zhang, N., Zheng, J., ... & Smith, K. J. (2015). Effect of preparation method on Ni2P/SiO2 catalytic activity for NaBH4 methanolysis and phenol hydrodeoxygenation. international journal of hydrogen energy, 40(46), 16137-16146.